Ab initio study of the thermodynamic properties of nonmagnetic elementary fcc metals: Exchange-correlation-related error bars and chemical trends

Blazej Grabowski, Tilmann Hickel, and Jörg Neugebauer
Max-Planck-Institut für Eisenforschung, D-40237 Düsseldorf, Germany
and Theoretische Physik, Universität Paderborn, D-33098 Paderborn, Germany
(Received 22 March 2007; revised manuscript received 5 June 2007; published 26 July 2007)

Thermal properties of an extensive set of fcc metals (Al, Pb, Cu, Ag, Au, Pd, Pt, Rh, and Ir) have been studied using density-functional theory in combination with the quasiharmonic approximation. Systematic convergence checks have been performed to ensure an accuracy greater than 1 meV/atom in the free energies. Phonon dispersion relations, Grüneisen parameters, free energies, thermal expansions, and heat capacities have been calculated for the two popular exchange-correlation functionals: Local density approximation and Perdew-Burke-Ernzerhof generalized gradient approximation [Phys. Rev. Lett. **77**, 3865 (1996)]. The results are found to be in excellent agreement with both experimental and CALPHAD data.

DOI: 10.1103/PhysRevB.76.024309 PACS number(s): 63.20.−e, 65.40.−b, 71.15.Mb

I. MOTIVATION

The collection of thermodynamically stable phases in the form of phase diagrams is one of the fundamental tools for engineers when determining processing routes (road maps[1]) to design materials. A well established approach for obtaining such phase diagrams is the CALPHAD (calculations of phase diagrams; Refs. 2 and 3) method. It is, however, based on experimental input and therefore suffers from the fact that the required sample preparation and high precision measurements are often challenging and expensive. Further, from a principle point of view, some necessary input (e.g., energetics of metastable phases) is missing due to the lack of corresponding samples. A possible approach to address these challenges is to employ *ab initio* methods to provide the missing experimental data.

A very promising tool is density-functional theory[4] (DFT), which has succeeded over the last decades in accurately predicting physical, chemical, and mechanical properties for a wide range of materials.[5] Based exclusively on fundamental physical concepts, no experimental input is needed. Solely the specific material has to be defined by providing the chemical species. The only (currently) uncontrollable approximation in DFT is the exchange-correlation (XC) functional, since its exact form is unknown and no practical way to systematically improve it exists.[6] Therefore, a critical evaluation of the predictive performance of XC functionals is crucial.[7–9]

As stated in a recent review,[10] the idea of coupling CALPHAD with *ab initio* methods has been debated almost since its original development. Traditionally, the main use of *ab initio* methods for CALPHAD calculations has been the computation of $T=0$ K energies.[11] This is due to the fact that DFT was originally developed as a ground state theory and its extension to $T>0$ K is accompanied by a heavy increase in computational effort, due to the dramatically increased phase space. However, in order to derive complete phase diagrams employing *ab initio* techniques, the extension to $T>0$ K is unavoidable and crucial.

The main contributions to the free energy determining the temperature dependence of phase stabilities of nonmagnetic alloys are electronic, configurational, and vibrational entropies. The electronic contribution can be taken into account with relatively low computational effort using the finite temperature extension to DFT developed by Mermin.[12] A fully coupled treatment of the configurational and vibrational contribution, which can be of equal magnitude,[13] is a formidable task. In order to calculate the configurational entropy contribution, two major approaches are used: The cluster expansion[14] and the coherent-potential approximation.[15]

An appealing approach to account for the vibrational entropy is the combination of DFT and the quasiharmonic approximation.[16–18] Within this approach, a set of *ab initio* calculated thermodynamic properties (phonon dispersion, thermal expansion, heat capacity) can be obtained and compared to experimental data. So far, such an extended comparison has been performed only for a few selected elements [e.g., Cu, Ag, Al].[8,16,17] Furthermore, except for Cu, these studies have been restricted to the local density approximation (LDA) XC functional and in none of these studies a comparison between the calculated results and CALPHAD results has been performed.

The aim of this paper is therefore to investigate a representative and extensive set of (nonmagnetic) materials having the same crystal structure. Specifically, we consider nine elementary face-centered-cubic (fcc) metals: Al, Pb, Cu, Ag, Au, Pd, Pt, Rh, and Ir. In order to provide a systematic basis for the evaluation of the accuracy and predictive power of common DFT functionals, we calculate phonon dispersions, thermal expansions, and heat capacities for the LDA and generalized gradient approximation (GGA) functional. Further, we compare our *ab initio* free energies to free energies obtained with the CALPHAD method. Our study follows in many aspects the pioneering work of Moruzzi *et al.*,[19] who performed a systematic study of fcc and bcc metals combining DFT-LDA and a Debye treatment of the lattice dynamics. The essential difference, however, is the replacement of the empirical Debye treatment by a fully consistent *ab initio* approach to treat the temperature dependence of the free energy.

II. THEORY

The basic quantity, from which we will derive all thermodynamic properties, is the free energy F as a function of the crystal volume V and the temperature T. For an elementary nonmagnetic crystal, electronic (el) excitations as well as ionic vibrations (vib) contribute to F and within the adiabatic approximation[20] F reads

$$F(V,T) = F^{\mathrm{el}}(V,T) + F^{\mathrm{vib}}(V,T). \tag{1}$$

Within finite temperature DFT,[12] F^{el} is given by

$$F^{\mathrm{el}} = E^{\mathrm{tot}}(T) - TS^{\mathrm{el}}, \tag{2}$$

where E^{tot} is the total energy of the crystal and S^{el} the electronic entropy.[21]

Within the harmonic approximation, F^{vib} per elementary (single atom) unit cell reads[20]

$$F^{\mathrm{vib}} = \frac{1}{N}\sum_{i}^{3N}\left\{\frac{1}{2}\hbar\omega_i + k_B T \ln\left[1 - \exp\left(-\frac{\hbar\omega_i}{k_B T}\right)\right]\right\}, \tag{3}$$

with the reduced Planck constant $\hbar$, the Boltzmann constant k_{B}, and phonon frequencies ω_i. The sum in Eq. (3) runs over the complete set of $3N$ phonon states, with N being the number of atoms inside the crystal cell obeying Born–von Karman periodic boundary conditions. The phonon frequencies ω_i are the eigenvalues of the dynamical matrix $\hat{D}$. For a periodic system, it is convenient to use the dynamical matrix in reciprocal space, which, for a crystal with a single basis atom, reduces to a 3×3 matrix with elements

$$D_{\mu,\nu}(\vec{q}) = \frac{1}{M}\sum_{I}^{N}\Phi_{I\mu,\nu}\exp[i\vec{q}\cdot\vec{R}_I]. \tag{4}$$

Here, M is the mass of the species, $\vec{q}$ is a wave vector within the Brillouin zone, $\vec{R}_I$ is a primitive unit-cell vector, μ and ν represent the three spatial dimensions x, y, and z, and $\hat{\Phi}$ is the force constant matrix consisting of elements

$$\Phi_{I\mu,\nu} = \frac{\partial^2 F^{\mathrm{el}}}{\partial u_{I\mu}\partial u_\nu} = \frac{\partial \tilde{F}^{\mathrm{HF}}_{I\mu}}{\partial u_\nu}, \tag{5}$$

with the displacement $u_{I\mu}$ of atom I in direction μ and the displacement u_ν in direction ν. $\tilde{F}^{\mathrm{HF}}_{I\mu}$ is the μth component of the Hellmann-Feynman force[22,23] acting on atom I. Due to translational symmetry, the displacement u_ν can be performed on an arbitrary but fixed atom in the crystal. For convenience, the chosen atom is shifted to the origin.

The electronic free energy F^{el} entering Eq. (5) depends on the volume and determines thus the volume dependence of the phonon frequencies and eventually of the vibrational free energy F^{vib} in Eq. (3). F^{el} also depends explicitly on the (electronic) temperature T via Eq. (2) and hence

$$F^{\mathrm{el}} = F^{\mathrm{el}}(V,T) \rightarrow \omega_i = \omega_i(V,T) \rightarrow F^{\mathrm{vib}} = F^{\mathrm{vib}}(V,T). \tag{6}$$

In principle, it would be straightforward to calculate this temperature dependence within DFT using Eq. (5). However, since we expect the effect of the electronic temperature on the force constant matrix to be small, we replace F^{el} by $E^{\mathrm{el}}(T=0\ \mathrm{K})$ in Eq. (5). This removes the explicit temperature dependence in the phonon frequencies: $\omega_i = \omega_i(V)$. This corresponds to the quasiharmonic approximation.

Having computed the thermodynamic potential $F(V,T)$, it can be utilized to determine all relevant thermodynamic material properties. For instance, the temperature dependence of the equilibrium volume $V_{\mathrm{eq}}(P,T)$ at a given pressure P can be obtained by finding a volume V_{eq}, which obeys the following condition:

$$-\left(\frac{\partial F(V,T)}{\partial V}\right)_{V=V_{\mathrm{eq}}} = P. \tag{7}$$

Using $V_{\mathrm{eq}}(P,T)$, the (implicit) pressure and temperature dependence of the phonon frequencies ω_i can be formulated. A further material property, which can be readily calculated, is the heat capacity[20] C_V at constant or fixed volume as well as C_P at constant pressure.

TABLE I. Plane wave energy cutoffs (in eV) employed in the total energy and force calculations.

Al	250
Rh	270
Ir	250
Pb	150
Pd	270
Pt	250
Cu	290
Ag	270
Au	250

III. METHOD

The total energy and force calculations have been performed within the projector-augmented wave[24] (PAW) plane wave approach. We have used the software package VASP (Ref. 25) in combination with the provided PAW potentials.[26] The plane wave energy cutoffs used in this study are listed in Table I. These choices ensure the free energy F to be converged to within 1 meV/atom. In order to evaluate the accuracy of the PAW potentials, we have additionally performed case studies with an all-electron method (WIEN2K,[27] see Sec. V A). For the XC functional, the LDA as well as the GGA have been considered. We have chosen the scheme of Ceperley and Alder[28] as parametrized by Perdew and Zunger[29] for LDA and the Perdew-Burke-Ernzerhof[30] (PBE) parametrization for GGA.

A. Electronic free energy

The electronic free energy F^{el} has been calculated employing the finite temperature formulation of DFT by Mermin.[12] Further, we have used the Monkhorst-Pack[31] scheme to sample the Brillouin zone. A mesh of $32\times 32\times 32$ k points (kp's) corresponding to 33×10^3 kp·atom[32] guarantees $F^{\mathrm{el}}(V,T)$ to be converged well below 1 meV/atom.

For the evaluation of the thermodynamic quantities, we have parametrized F^{el} with respect to V and T. In particular, we have found a separation of F^{el} into the total energy $E^{\mathrm{tot}}(V)$ at $T=0$ K and a remaining part $\bar{F}$ with a linear dependence on V most suitable:

$$F^{\mathrm{el}}(V,T) = E^{\mathrm{tot}}(V, T=0\ \mathrm{K}) + \bar{F}^{\mathrm{el}}(V,T). \tag{8}$$

Interpolating $\bar{F}^{\mathrm{el}}$ linearly in V,

$$\bar{F}^{\mathrm{el}}(V,T) = a^{\mathrm{el}}(T) + b^{\mathrm{el}}(T)V, \tag{9}$$

gives an error well below 1 meV/atom within the volume range considered in this study. The temperature dependence of a^{el} and b^{el} has been parametrized by fitting to fourth-order polynomials in T:

$$a^{\mathrm{el}}(T) = \sum_{i=1}^{4} \alpha_i T^i, \quad b^{\mathrm{el}}(T) = \sum_{i=1}^{4} \beta_i T^i. \tag{10}$$

The total energy $E^{\mathrm{tot}}(V, T=0\ \mathrm{K})$ has been parametrized by a least-squares fit to the Murnaghan equation of state:[33]

$$E(V) = E(V_{\mathrm{eq}}) + \frac{BV}{B'^2 - B'}[B'(1-x) + x^{B'} - 1]. \tag{11}$$

Here, $x = V_{\mathrm{eq}}/V$. V_{eq} is the equilibrium volume [in the following, we also use the equilibrium lattice constant, which for the considered cases is given by $a=(4V_{\mathrm{eq}})^{1/3}$], $B=-V(\partial P/\partial V)_T$ the bulk modulus, and B' its derivative with respect to pressure. In Eq. (11), V_{eq}, B, and B' correspond to $P=0$ Pa.

B. Vibrational free energy

The force constant matrix $\hat{\Phi}$ has been calculated using the (direct) force constant method[34] (also referred to as the small displacement method[35,36]). A displacement of 0.0053 Å (0.01 Bohr radius) has been used to obtain the Hellmann-Feynman forces. This choice ensures that the forces on all atoms in the supercell are linear with respect to the displacement. As pointed out in Sec. II, $\hat{\Phi}$ has been calculated with respect to $E^{\mathrm{el}}(T=0\ \mathrm{K})$ rather than $F^{\mathrm{el}}(T)$. For that purpose, we have replaced the Fermi-Dirac broadening with the Methfessel-Paxton scheme[37] in first order. A broadening parameter of 0.1 eV ensures that the fictitious electronic entropy term does not exceed the value of 1 meV/atom (see Ref. 38). For the Brillouin zone sampling of the electronic dispersion, we have used 7×10^3 kp·atom ($3\times3\times3$ kp mesh; 256 atoms) for the transition metals, 16×10^3 kp·atom ($4\times4\times4$ kp mesh; 256 atoms) for Al, and 32×10^3 kp·atom ($4\times4\times4$ kp mesh; 500 atoms) for Pb, resulting in F^{vib} converged to ~1 meV/atom (see Sec. IV B).

The convergence criterion for the electronic loop has been set to 10^{-7} eV. The mesh size for the calculation of the augmentation charges has been set to 432×10^3 grid points/atom (see Sec. IV A). We have used a $5\times5\times5$ (henceforth abbreviated by 5^3) supercell (in units of the conventional fcc unit cell consisting of four atoms) for Pb and 4^3 supercells for the other elements (see Sec. IV C). For the calculation of averaged quantities depending on the full phonon dispersion $\omega(\vec{q})$ inside the Brillouin zone, we have used an equidistantly spaced q-point mesh of dimensions $16\times16\times16$. Finally, in analogy to F^{el}, we have also parametrized F^{vib} linearly in V,

$$F^{\mathrm{vib}}(V,T) = a^{\mathrm{vib}}(T) + b^{\mathrm{vib}}(T)V, \tag{12}$$

with the T dependence given analytically by Eq. (3). All these choices have been carefully checked to give errors in the free energy well below 1 meV/atom for all elements investigated in this study.

IV. CONVERGENCE CHECKS: SPECIAL TOPICS

In order to perform a critical evaluation of the predictive power of XC functionals, it is important to rule out the influence of further (controllable) approximations. Since some parameters strongly affect thermodynamic quantities, careful convergence checks with respect to these values turned out to be crucial. Below, we describe selected checks, with a focus on the GGA functional. Case studies with the LDA functional yield similarly converged results.

In order to quantify the rate of convergence, we will focus on two quantities: The vibrational free energy F^{vib} and the averaged (phonon) Grüneisen parameter[20] γ defined as

$$\gamma = -\frac{V}{3N}\sum_{i}^{3N}\frac{1}{\omega_i}\frac{d\omega_i(V)}{dV}. \tag{13}$$

A high accuracy of γ is crucial, since an error in γ produces an error of the same order of magnitude in b^{vib} [Eq. (12)] and thus affects the resulting thermodynamic properties. Both quantities have been computed at the equilibrium volume at $P=0$ Pa and $T=0$ K. F^{vib} has been calculated at a fixed temperature of $T=400$ K. In the following, the convergence rate is shown relative to the converged (conv) values. Absolute values of F^{vib} and γ at these conditions can be inferred from Fig. 9.

For two convergence parameters, the k-point mesh and the supercell size, we will additionally discuss their effect on the phonon dispersions $\omega(\vec{q})$.

A. Grid for augmentation charges

A quantity we have identified to be crucial for achieving a high accuracy in thermodynamic calculations is the size of the grid used to calculate the augmentation charges (henceforth labeled "augGrid") in the PAW method employed here. To allow a proper investigation of the augGrid, we have performed the augGrid convergence tests by keeping the well converged cutoffs from Table I fixed. This decouples the augGrid from the grid used to store the wave function and charge density coefficients (henceforth labeled "basicGrid"), which is determined by the plane wave energy cutoff.

The influence of the augGrid size on γ is demonstrated in Fig. 1 for two elements with hard, i.e., strongly localized, augmentation charges, Cu and Ag. The example of Cu shows that working with an augGrid eight times larger than the basicGrid[39] (line L_1 in Fig. 1) results in a −10.3% error in the γ value. Even by making the augGrid 64 times larger than

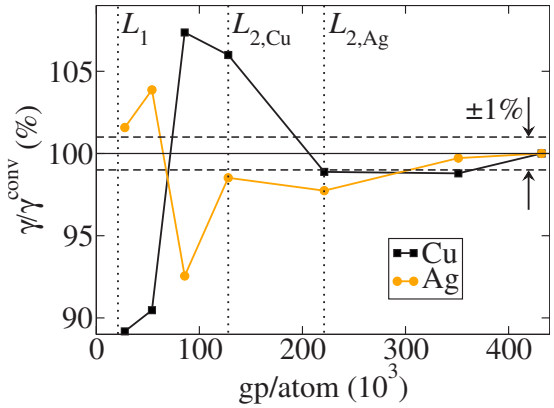

FIG. 1. (Color online) Convergence of the averaged Grüneisen parameter γ with respect to the augGrid (see text) in terms of grid points per atom (gp/atom) for Cu and Ag. The lines L_1 (similar for Cu and Ag on this scale) and $L_{2,Cu/Ag}$ correspond to grid sizes being 8 and 64 times larger than the basic grid at a converged cutoff (see Table I). The values were obtained using a 3^3 supercell and a kp mesh of 7×10^3 kp·atom.

the basicGrid[40] (line L_2 in Fig. 1), the error reduces only slightly (7.1%). In the case of Ag, the larger equilibrium lattice constant yields a larger basicGrid. For this case, an augGrid 64 times larger than the basicGrid reduces the error in γ to −1.4%.

A direct calculation of the augGrid convergence rate employing a well converged supercell size for all investigated elements is computationally highly expensive. Using, for instance, a 3^3 supercell (see Sec. IV C) for all elements would require more than 10 000 CPU hours on an AMD Opteron with a clock speed of 2.4 GHz.

We have therefore employed a scaling procedure, which allows an efficient and accurate determination of the convergence rate. The key idea of this approach is as follows: Let us assume a physical target quantity α and two convergence parameters c_1 and c_2. We are interested in the convergence rate of α with respect to c_1 at a converged value of $c_2=c_2^{conv}$, i.e., $\alpha(c_1,c_2^{conv})$. For most cases, computing $\alpha(c_1,c_2^{conv})$ directly is highly expensive. However, we have found that in many cases the following approximation can be utilized to obtain an accurate description of $\alpha(c_1,c_2^{conv})$:

$$\alpha(c_1,c_2^{conv}) \approx \alpha(c_1^a,c_2^{conv}) + s\Delta\alpha,$$

$$\Delta\alpha = \alpha(c_1,c_2^{small}) - \alpha(c_1^a,c_2^{small}). \quad (14)$$

Here, s is a scaling parameter defined as

$$s = \frac{\alpha(c_1^b,c_2^{conv}) - \alpha(c_1^a,c_2^{conv})}{\alpha(c_1^b,c_2^{small}) - \alpha(c_1^a,c_2^{small})} \quad (15)$$

and c_1^a, c_1^b ($c_1^a \neq c_1^b$), and c_2^{small} are fixed (but not fully converged) parameters. The idea is then to study in a first step the convergence of $\alpha(c_1,c_2^{small})$ in detail. Therefore, c_2^{small} is chosen to provide a computationally inexpensive calculation. In a second step, the scaling parameter s is calculated by performing only two (expensive) calculations for c_2^{conv}: $\alpha(c_1^a,c_2^{conv})$ and $\alpha(c_1^b,c_2^{conv})$. Finally, $\alpha(c_1,c_2^{conv})$ is approximated by Eq. (14).

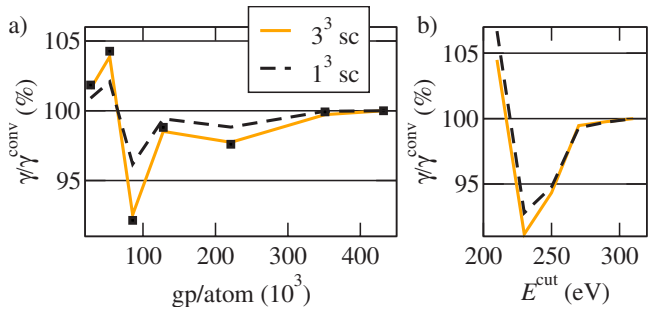

FIG. 2. (Color online) (a) AugGrid convergence of the averaged Grüneisen parameter γ for Ag for the 1^3 and 3^3 supercells (sc). The black squares show the convergence of the 1^3 sc after rescaling it using Eq. (14). (b) Similar to (a) but with the plane wave energy cutoff E^{cut} as the convergence parameter.

To be more specific, let us consider α to be the averaged Grüneisen parameter γ, c_1 to be the augGrid size, and c_2 to be the supercell size. Further, c_2^{small} corresponds to a 1^3 supercell and c_2^{conv} to a 3^3 supercell. We set $c_1^a=28\times10^3$ grid points/atom (gp/atom) and $c_1^b=54\times10^3$ gp/atom. As a representative example, Fig. 2(a) shows the results we have obtained for Ag. As can be seen, the computed values closely follow the scaling relation according to Eq. (14). Thus, to obtain a densely sampled convergence study for large supercells, only two expensive calculations are needed and a gain in computational efficiency of at least 1 order of magnitude can be easily achieved.

We have studied how the scaling parameter depends on the chemical species and the supercell size. Our results show a small chemical dependence (<10%). The supercell size dependence shows a significant scaling parameter only when increasing a 1^3 to a 2^3 supercell. We have also verified that the same approach can be applied to determine the plane wave energy cutoff convergence of large supercells [Fig. 2(b)]. For this case, a scaling parameter generally close to 1 is found.

The convergence rate of γ with respect to the augGrid size is summarized in Fig. 3 for all metals studied here. For some of the elements, we had to extend the range of the augGrid sizes to even larger values than shown in Fig. 1. An inspection of Fig. 3 shows that the convergence rate correlates inversely with the hardness (localization) of the augmentation charge of the specific element: Among the transition metals, γ converges slower when filling up the d shell and when reducing the atomic radius. Thus, Cu, having the hardest augmentation charge, is the most sensitive element. In contrast, Al and Pb, where only s and p electrons form the chemical bonds, exhibit a relatively low dependence on the augGrid.

B. *k*-point sampling

A second convergence parameter, which we have found to be crucial in predicting thermodynamic properties of metals with extremely high accuracy, is the kp sampling of the elec-

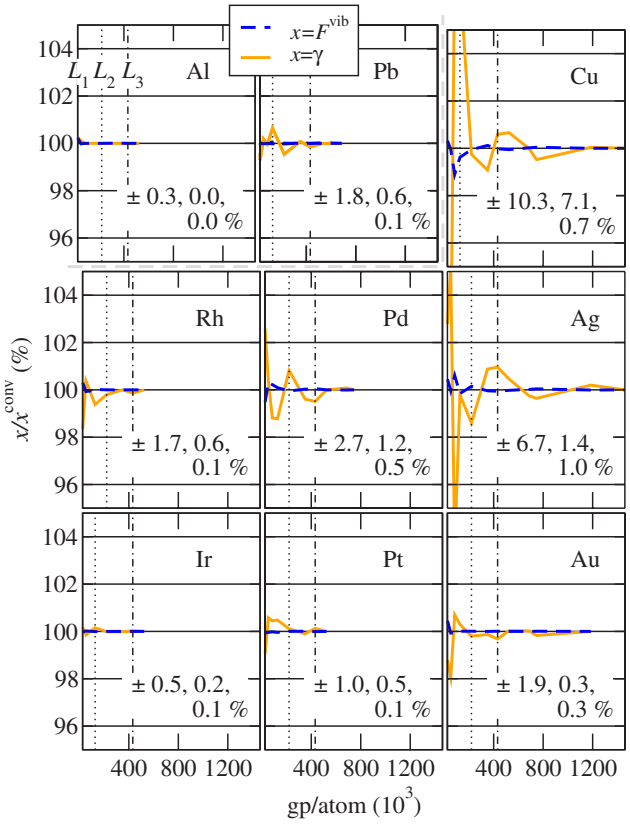

FIG. 3. (Color online) AugGrid convergence of the averaged Grüneisen parameter γ and the vibrational free energy F^{vib} for all investigated elements. The lines L_1 (falls together with the y axis on this scale) and L_2 (dashed line) are defined as in Fig. 1. Line L_3 (dot-dashed line) corresponds to the augGrid size used in the present study (Sec. V). The numbers inside each graph show the error range of the Grüneisen parameter at line L_1, L_2, L_3. The values have been obtained using a kp mesh of 7×10^3 kp·atom and a 1^3 supercell. The scaling procedure [Eq. (14)] has been employed to rescale the values to correspond to large supercells. Al and Pb are separated to distinguish them from the transition metals.

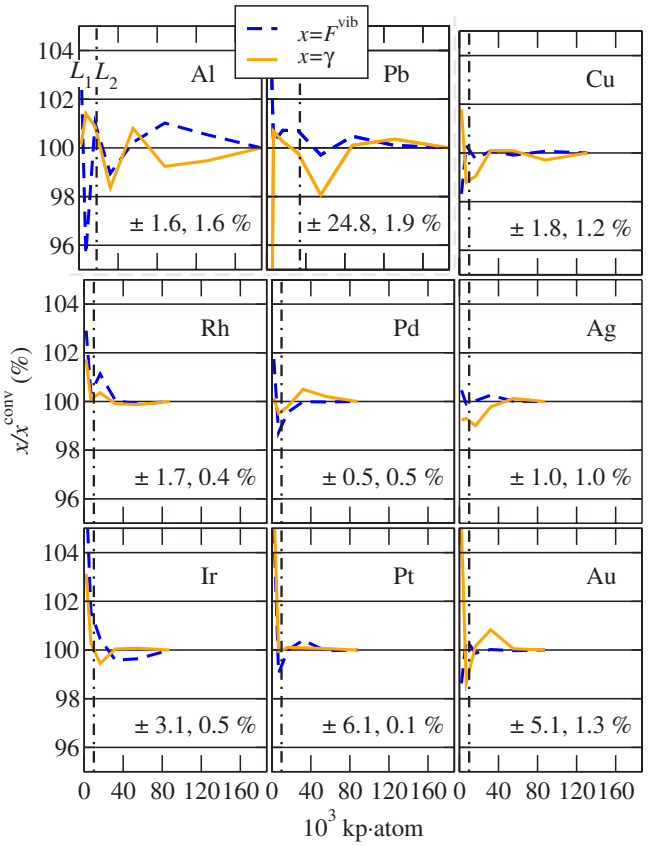

FIG. 4. (Color online) kp convergence of the averaged Grüneisen parameter γ and the vibrational free energy F_{vib} for all investigated elements. The line L_1 (falls together with the y axis on this scale) corresponds to the smallest investigated kp mesh of 2×10^3 kp·atom and the line L_2 (dot-dashed line) to the kp meshes used for the calculations presented in Sec. V. The numbers inside each graph show the error range of γ at lines L_1, L_2. The values have been obtained using a 2^3 supercell.

tronic dispersion within the Brillouin zone. To systematically investigate the kp-sampling dependence of γ and F^{vib}, we utilize again the scaling approach [Eq. (14)]. In this case, starting from a 1^3 supercell [parameter c_2^{small} in Eq. (14)] is not sufficient to guarantee a reasonable approximation, but a 2^3 supercell is needed. The scaling parameter is ~ 1.

The results of the convergence study are shown in Fig. 4. The main conclusion is that Al and Pb exhibit a strikingly worse convergence behavior for γ and F^{vib} than the transition metals. For Al, the convergence of both quantities shows a significant gradient even at the largest considered kp mesh (190×10^3 kp·atom). Hence, in contrast to all other elements, the given error bar for the averaged Grüneisen parameter of Al has to be taken with care. For Pb, the smallest kp sampling considered here of 2×10^3 kp·atom yields an error in γ as large as -25%.

In addition to the convergence of the averaged quantities, γ and F^{vib}, we have analyzed in detail the convergence of the phonon dispersion $\omega(\vec{q})$. For this convergence study, shown in Fig. 5, the 4^3 supercell has been used. The results will be discussed for three representative cases.

Among the transition metals, the dispersion of Ir shows the slowest convergence. Nevertheless, the convergence is rapid and no qualitative changes are observed. In contrast to all transition metals, the convergence of Al and Pb is more complex: For some kp meshes, an anomalous behavior in the vicinity of the Γ point appears (indicated by the circles in Fig. 5). In these regions, the phonon frequencies are imaginary. For convenience, the imaginary frequencies are shown as negative frequencies in Fig. 5.

In principle, the presence of imaginary frequencies indicates that the structure is unstable against deformations along the corresponding phonon wave vector. The imaginary frequencies found for some kp samplings are, however, not related to a genuine structural instability, but are unphysical and caused by not fully converged parameters. In the case of Al, the instability occurring at 7×10^3 kp·atom can be removed by enlarging the kp sampling to 16×10^3 kp·atom, while for Pb, the instability is more persistent and occurs even for large samplings (16×10^3 kp·atom). To ensure that the instability is not caused by a too small kp sampling, we

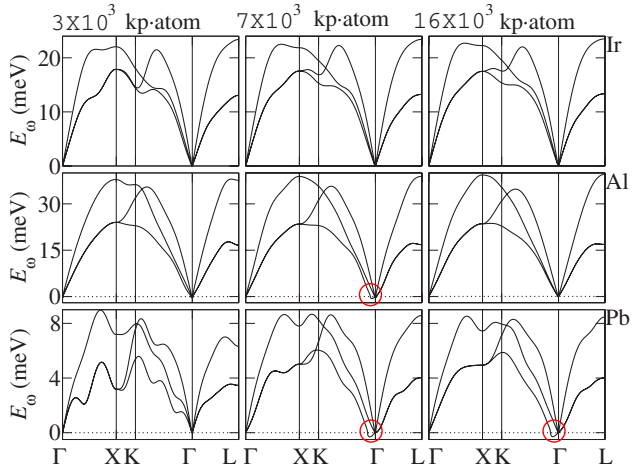

FIG. 5. (Color online) kp convergence of the phonon dispersion $\omega(\vec{q})$ ($E_\omega=\hbar\omega$ with $\hbar$ the Planck constant) along some high symmetry directions for Ir, Al, and Pb for the 4^3 supercell. The red circle marks unphysical phonon instabilities (imaginary frequencies; see text).

have further increased the kp sampling (55×10^3 kp·atom; not shown), but found no changes in the phonon dispersion. In Sec. IV C, it will be shown that the instability is indeed fictitious; however, it is not related to the kp convergence but to a (still) insufficient supercell size.

The occurrence of imaginary frequencies due to insufficient convergence requires special care when calculating thermodynamic quantities. A possible approach would be to calculate the thermodynamic quantities exclusively for highly converged parameters, for which the unphysical instability is fully absent. However, even in the presence of these instabilities sufficiently converged thermodynamic quantities can be obtained by neglecting all imaginary frequencies when calculating F^{vib} according to Eq. (3). We have found this approximation to have little effect on the free energy and derived quantities in most cases, since the phase space around the Γ point is negligible compared to the full Brillouin zone. An example of how well this approach works is given in the following section in Fig. 8, where the convergence of γ and F^{vib} for Al, Pb, and Pd has been calculated using this approach.

C. Supercell size

Let us now focus on the remaining critical convergence parameter, the supercell size. An extensive analysis for all elements shows a qualitatively similar behavior as for the kp sampling. In particular, for Pd and Pb certain (unconverged) supercell sizes give rise to an unphysical phonon instability in the vicinity of the Γ point.

The supercell size convergence of the phonon dispersion for Pd is shown in Fig. 6 for the 2^3, 3^3, and 4^3 supercell. Figure 6 reveals that using a 2^3 supercell results in a "well-behaved" phonon dispersion without any instabilities. Thus, one might be easily misled and consider these results as converged. However, increasing the supercell size to 3^3, a small instability occurs in the vicinity of the Γ point along the L direction and a larger one along the X direction. The instability disappears again for the 4^3 supercell.

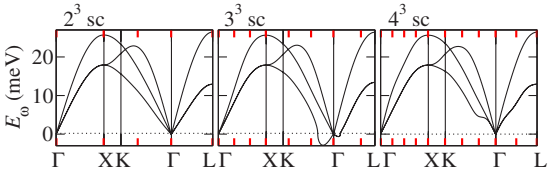

FIG. 6. (Color online) Supercell (sc) size convergence of the phonon dispersion for Pd using a k-point mesh of 7×10^3 kp·atom. The red ticks mark the exact q points (see text) for the specific supercell.

A closer inspection of this feature reveals that it is caused by an intricate interplay between the sampling of the phonon Brillouin zone and the occurrence of anomalies in the phonon dispersion as a consequence of long-range interactions. The sampling of the phonon Brillouin zone is determined and restricted by the size of the supercell. For the investigated elements, a supercell consisting of N atoms can represent only N phonon wave vectors $\vec{q}$. These are commonly termed exact q points.[34] At these points, marked in Fig. 6 by red ticks, the phonon frequencies are exact, i.e., these frequencies would also be obtained for a (large) fully converged supercell. Frequencies at the remaining (nonexact) q points are merely interpolated by a Fourier expansion with a limited q basis set and may change and/or improve when increasing the supercell size.

For the case of the large 4^3 Pd supercell (Fig. 6), the q-point mesh is sufficiently fine to resolve the anomaly, which has also been observed experimentally (see Ref. 41 and Fig. 11). For the 3^3 supercell, the q-point mesh is too coarse to fully resolve the anomaly. Nevertheless, the exact q point next to the Γ point is strongly affected by the anomaly and causes the q interpolation to make a "dip" with imaginary frequencies in between the two exact q points. The exact q mesh for the 2^3 supercell is so coarse that the exact q point neighboring Γ is too far away to be affected by the anomaly.

For Pb, the supercell size convergence of the phonon dispersion (Fig. 7) shows no phonon instability for the 2^3 and 3^3 supercells. Increasing the size to 4^3, an instability occurs in the same region as for Pd. The magnitude of the instability is, however, significantly smaller. Increasing the supercell size further to 5^3 (corresponding to 500 atoms) almost completely removes the imaginary frequencies. We expect a complete disappearance of the imaginary frequencies when going to even larger supercells, since previous calculations[42] based on the linear response method and experiment[41] report no instability.

The convergence of the averaged quantities γ and F^{vib} is shown in Figs. 8 and 9 for all investigated elements. In Fig. 8, it becomes apparent that there is a significant increase in the quality of both quantities for almost all elements when enlarging the supercell to the size of 2^3. In contrast, the supercells 2^3, 3^3, and 4^3 yield similar values with a scattering of about ±2%. Moreover, the convergence of both quantities exhibits a satisfactory behavior for most elements (Pt being one exception), i.e., the slope in the error dependence de-

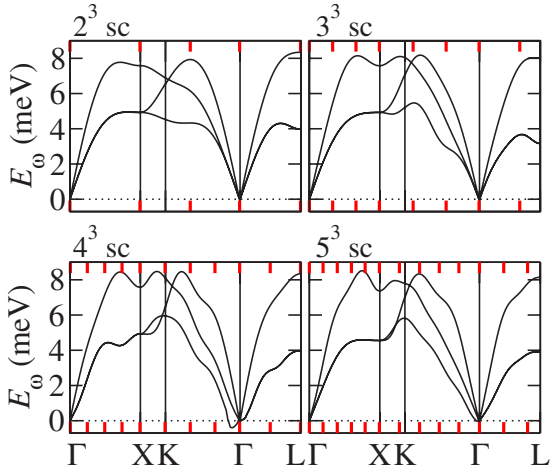

FIG. 7. (Color online) Supercell (sc) size convergence of the phonon dispersion for Pb. The k-point mesh size was 32×10^3 kp·atom for the 5^3 supercell and 7×10^3 kp·atom for the other supercells. Exact q points are marked by red ticks.

creases monotonously with the supercell size.

Figure 9 shows the supercell size convergence of the absolute theoretical values of γ and F^{vib}. It also includes experimental data of γ obtained from C_V data. As can be seen,

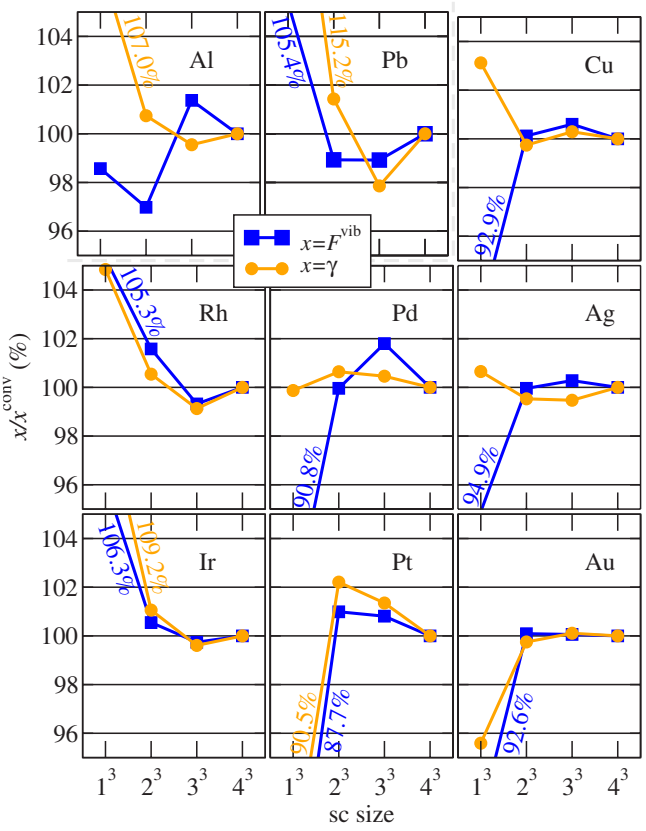

FIG. 8. (Color online) Supercell (sc) size convergence of the averaged Grüneisen parameter γ and the vibrational free energy F_{vib} for all investigated elements. The k-point mesh is 7×10^3 kp·atom for all elements. The numbers in the graphs show values for the 1^3 supercell when the corresponding data point lies outside the graph.

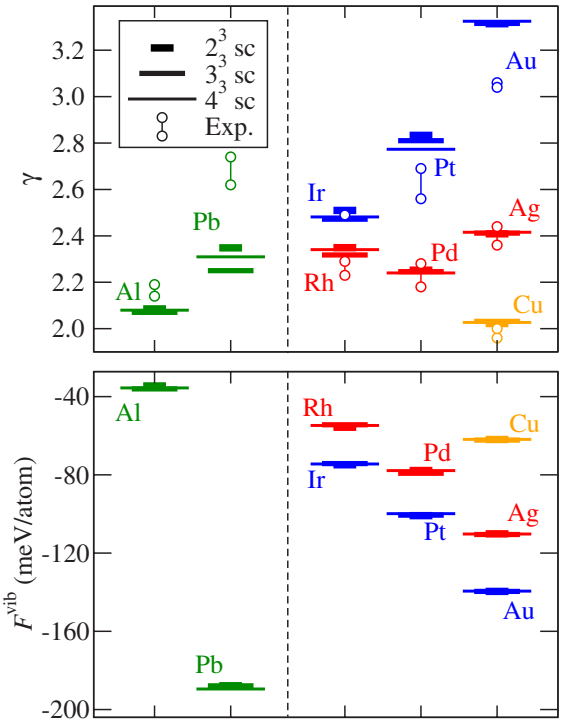

FIG. 9. (Color online) Supercell (sc) size convergence of the averaged Grüneisen parameter γ and the vibrational free energy F_{vib} (at T=400 K) in absolute values for all investigated elements. The used k-point mesh was 7×10^3 kp·atom for all elements. Transition metals in the same row in the Periodic Table are given the same color. Al and Pb are separated for reading convenience. The experimental data are taken from Ref. 43.

for most elements the theoretical error bars due to convergence are smaller than the scattering in the experimental data. Actually, including all available experimental data of γ (e.g., obtained from compressibility or shock wave experiments; not shown here) would significantly increase the interval of experimental scatter.[43] We note, however, that a comparison between the theoretical and experimental γ values should be taken with care, since they are derived from different definitions. The theoretical Grüneisen parameter [Eq. (13)] containing only vibrational contributions is an average over all q-dependent Grüneisen parameters. The experimental γ, shown in Fig. 9, is a derived quantity from the heat capacity at constant volume and corresponds to the theoretical one only if the approximate Mie-Grüneisen equation of state is valid.[44,45] Further, the experimental data contain additionally an electronic contribution, which is negligible for Al, Cu, Ag, and Au, has a value of ~0.1 for Rh, Ir, and Pb, and has a value of ~0.2 for Pd and Pt.[43]

V. COMPARISON BETWEEN THEORY AND EXPERIMENT

A. Potential and free energy at T=0 K

The T=0 K energy-volume dependence [$E^{\mathrm{tot}}(V,T=0\ \mathrm{K})$; Eq. (8)] has been calculated for all elements and fitted to the Murnaghan equation of state [Eq. (11)]. The results obtained from the fits for the equilibrium lattice constant a, bulk

TABLE II. Results for the equilibrium lattice constant a, bulk modulus B, and its derivative with respect to pressure B' at $T=0$ K and $P=0$ Pa for the projector-augmented wave (PAW) and all-electron (ae) approach. The index e (i) indicates whether zero-point vibrations are excluded (included). The deviation from experiment is labeled Δa_i and ΔB_i. All-electron values marked with an asterisk are estimated values obtained using the (relative) zero-point contributions from the PAW results. All experimental lattice constants are taken from Ref. 47 ($T=5$ K). The experimental bulk moduli are taken from Ref. 20 (low temperature values) for Al, Pb, Cu, Ag, and Au and from Ref. 48 (Pd, $T\rightarrow 0$ K), Ref. 49 (Rh, $T\rightarrow 0$ K), and Ref. 50 (Pt, Ir, $T\rightarrow 0$ K). The available experimental B' are taken from Ref. 51 (collection of experimental $T\rightarrow 0$ K data).

	Al					Pb					Cu				
	LDA			GGA		LDA			GGA		LDA			GGA	
	ae	PAW	Exp.	ae	PAW	ae	PAW	Exp.	ae	PAW	ae	PAW	Exp.	ae	PAW
a_e (Å)	3.987	3.986		4.044	4.041	4.881	4.875		5.047	5.030	3.522	3.524		3.638	3.637
a_i (Å)	4.001*	3.999	4.032	4.057*	4.054	4.885*	4.879	4.905	5.052*	5.034	3.529*	3.530	3.602	3.645*	3.644
Δa_i (%)	−0.8*	−0.8		0.6*	0.6	−0.4*	−0.5		3.0*	2.6	−2.0*	−2.0		1.2*	1.2
B_e (GPa)	81	84		76	77	52	53		39	40	188	183		141	136
B_i (GPa)	78*	80	79	73*	74	51*	52	49	39*	40	183*	178	142	137*	132
ΔB_i (%)	−1.8*	1.3		−7.4*	−6.3	13.2*	15.6		−13.5*	−11.1	28.5*	25.4		−3.4*	−7.0
B'	4.3	4.6	4.7	4.3	4.7	4.7	5.0	5.5	4.2	5.6	5.1	5.1	5.3	5.1	5.1
	Rh					Pd					Ag				
	LDA			GGA		LDA			GGA		LDA			GGA	
	ae	PAW	Exp.	ae	PAW	ae	PAW	Exp.	ae	PAW	ae	PAW	Exp.	ae	PAW
a_e (Å)	3.762	3.767		3.839	3.842	3.847	3.854		3.949	3.954	4.008	4.016		4.152	4.165
a_i (Å)	3.766*	3.770	3.798	3.844*	3.847	3.851*	3.858	3.879	3.954*	3.959	4.014*	4.022	4.061	4.159*	4.172
Δa_i (%)	−0.8*	−0.7		1.2*	1.3	−0.7*	−0.5		1.9*	2.1	−1.2*	−1.0		2.4*	2.7
B_e (GPa)	321	313		260	252	230	223		169	165	140	136		91	88
B_i (GPa)	316*	308	269	255*	248	226*	219	195	166*	162	137*	133	109	89*	86
ΔB_i (%)	12.8*	10.0		−8.8*	−11.4	20.2*	16.5		−11.5*	−13.8	26.8*	23.1		−17.6*	−20.4
B'	5.3	5.2		5.4	5.3	5.7	5.5		5.7	5.7	5.8	5.7	5.9	5.8	5.9
	Ir					Pt					Au				
	LDA			GGA		LDA			GGA		LDA			GGA	
	ae	PAW	Exp.	ae	PAW	ae	PAW	Exp.	ae	PAW	ae	PAW	Exp.	ae	PAW
a_e (Å)	3.819	3.819		3.879	3.877	3.900	3.906		3.976	3.977	4.054	4.062		4.163	4.174
a_i (Å)	3.822*	3.821	3.835	3.882*	3.880	3.903*	3.909	3.909	3.978*	3.980	4.057*	4.066	4.065	4.167*	4.179
Δa_i (%)	−0.3*	−0.3		1.2*	1.2	−0.2*	0.0		1.8*	1.8	−0.2*	0.0		2.5*	2.8
B_e (GPa)	406	401		349	342	308	301		246	245	193	189		139	134
B_i (GPa)	402*	397	366	345*	338	304*	297	288	243*	242	190*	186	180	136*	131
ΔB_i (%)	8.7*	7.3		−6.8*	−8.6	4.7*	2.4		−16.3*	−16.6	5.1*	2.8		−25.0*	−27.6
B'	5.2	5.1		5.2	5.2	5.5	5.5		5.4	5.6	5.9	5.8	5.9	6.0	6.0

modulus B, and its derivative with respect to pressure B' are listed in Table II. The subscript e indicates that zero-point vibrations are excluded. Reference calculations for the $T=0$ K energy surface performed with an all-electron method [WIEN2K (Ref. 27) (L)APW+lo: (linearized) augmented plane wave + local orbital[46]] show only negligible deviations from the PAW calculations (see Table II).

A direct comparison between values excluding zero-point vibrations and experimental data being extrapolated to $T=0$ K would neglect that the experimental data correspond to a free energy at $T=0$ K, $F(V,T=0\ \text{K})$, and thus contain a contribution due to zero-point vibrations. To estimate the influence of zero-point vibrations, we have calculated the $T=0$ K free energy and parametrized $F(V,T=0\ \text{K})$ using Eq.

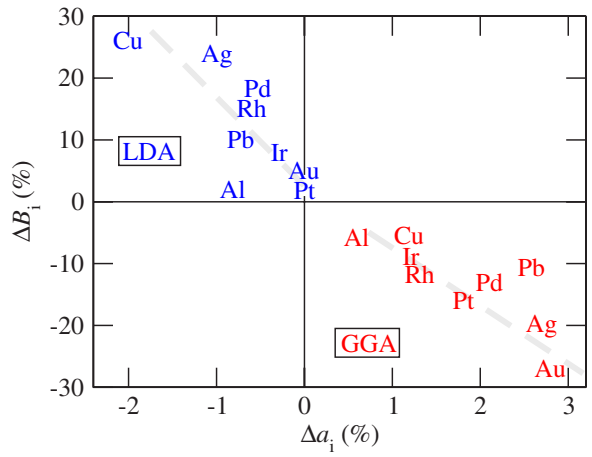

FIG. 10. (Color online) Correlation between the deviation from experiment for the lattice constants Δa_i and the bulk moduli ΔB_i (Table II). All quantities contain the influence of zero-point vibrations. The dashed lines are a guide for the eye and emphasize the linear trend for each functional.

(11). The results are given in Table II (indexed with a subscript i).

Table II shows that including zero-point vibrations has only a minor effect on the lattice constant. The average change is ~0.1%. For the bulk modulus, the effect is significantly stronger (~2%). In particular, the Al GGA bulk modulus softens considerably by about 4%. In general, the inclusion of zero-point vibrations improves (worsens) the agreement between the LDA (GGA) results and experiment.

In principle, the experimental ambient pressure conditions (100 kPa) should also be taken into account for a fully consistent comparison with experiment. However, the effect of pressure on the lattice constant and bulk modulus is consistently found to be more than an order of magnitude smaller than the changes due to zero-point vibrations. Therefore, we discuss here and in the following sections only values obtained at 0 Pa.

The comparison between experiment and theory shows that LDA (GGA) underestimates (overestimates) the experimental value of the lattice constant a and overestimates (underestimates) the value of the bulk modulus B. This behavior is a well established trend observed in numerous previous studies. For the set of metals investigated in this study, we find that LDA underestimates a on average by −0.7% and GGA overestimates it on average by 1.8%. The error in B, which is a second-order derivative, is much larger in magnitude (LDA average, 11.6%; GGA average, −13.7%) and inversely correlated to the error in a (Fig. 10). The inverse relation can be explained by the volume dependence of the total energy [Eq. (11)] causing a monotonous decrease of B with increasing volume. Particularly for GGA, an increase of the error with the number of d electrons among the $4d$ and $5d$ transition metals is apparent.

B. Phonon dispersion

In order to allow an accurate and consistent comparison between the experimental and our theoretical phonon dispersions, the theoretical phonon dispersions have to be computed at the experimental temperature. We have therefore calculated temperature dependent phonon dispersions. The results are shown in Fig. 11.

Generally, both functionals show a good agreement with experimental data. LDA, yielding larger phonon frequencies than GGA, overestimates the experimental data in most cases, while GGA underestimates it. A major conclusion we can therefore draw is that the LDA (GGA) results can be considered as an upper (lower) limit with respect to experimental data and thus as error bars for theoretical calculations. Small deviations between LDA and GGA, as, e.g., for Al, thus indicate small error bars and hence a high predictive power, while larger deviations as for Ag or Au indicate lower prediction accuracy.

The phonon dispersion of Cu, Ag, and Au is comparatively "simple" and can be described accurately already with nearest neighbor interactions. The dispersion of these elements has been the subject of previous theoretical studies [Cu,[8,9,52,53] Ag,[16] and Au (Refs. 54 and 55)]. For Ag and Au, however, only the LDA formalism has been used. The available data from the literature are in good agreement with our results.

The remaining elements exhibit more complex phonon dispersions. Anomalies, i.e., deviations from the simple dependence, are caused by interactions of the phonons with the electronic Fermi surface. To resolve these anomalies in the phonon dispersion, force constants including long-range interatomic interactions need to be captured, i.e., large supercells are crucial. As pointed out in Ref. 56, the dispersion relations of these elements "constitute a severe test for any theoretical treatment."

We first focus on Pd and Pt. The anomalies in the vicinity of the Γ point (enlarged in the insets of Fig. 11) have been attributed to virtual Kohn transitions.[41] Figure 11 shows that the anomalies are strong for the GGA-calculated dispersions, whereas the LDA-calculated dispersions show almost no deviation from linearity. In order to identify why LDA behaves differently, we have repeated the calculations of the phonon dispersion at the same (experimental) lattice constant for LDA and GGA. For Pt, both functionals yield under these conditions a comparable anomaly. We therefore conclude that for Pt the XC-functional dependence is mainly related to an effect of the atomic structure on the Fermi surface rather than due to changes in the Fermi surface caused by LDA and/or GGA. For Pd, however, this argument does not hold, since calculating the phonon dispersion at the same lattice constant yields a stronger pronounced anomaly for GGA than for LDA. Previous theoretical studies on Pd (Refs. 52 and 57) based on the linear response method have not reported the anomaly. However, in a recent theoretical study[58] on the electron-phonon coupling in Pd, the anomaly has been resolved and correlated to a distinct peak in the phonon linewidths.

The phonon dispersion of Rh and Ir shows anomalies in almost all branches. These pronounced anomalies originate from sharp peaklike features (caused by the d states) in the electronic Fermi surface. Both elements have been the subject of only a few experimental and theoretical (LDA) investigations.[56,59,60] Our LDA phonon dispersions agree

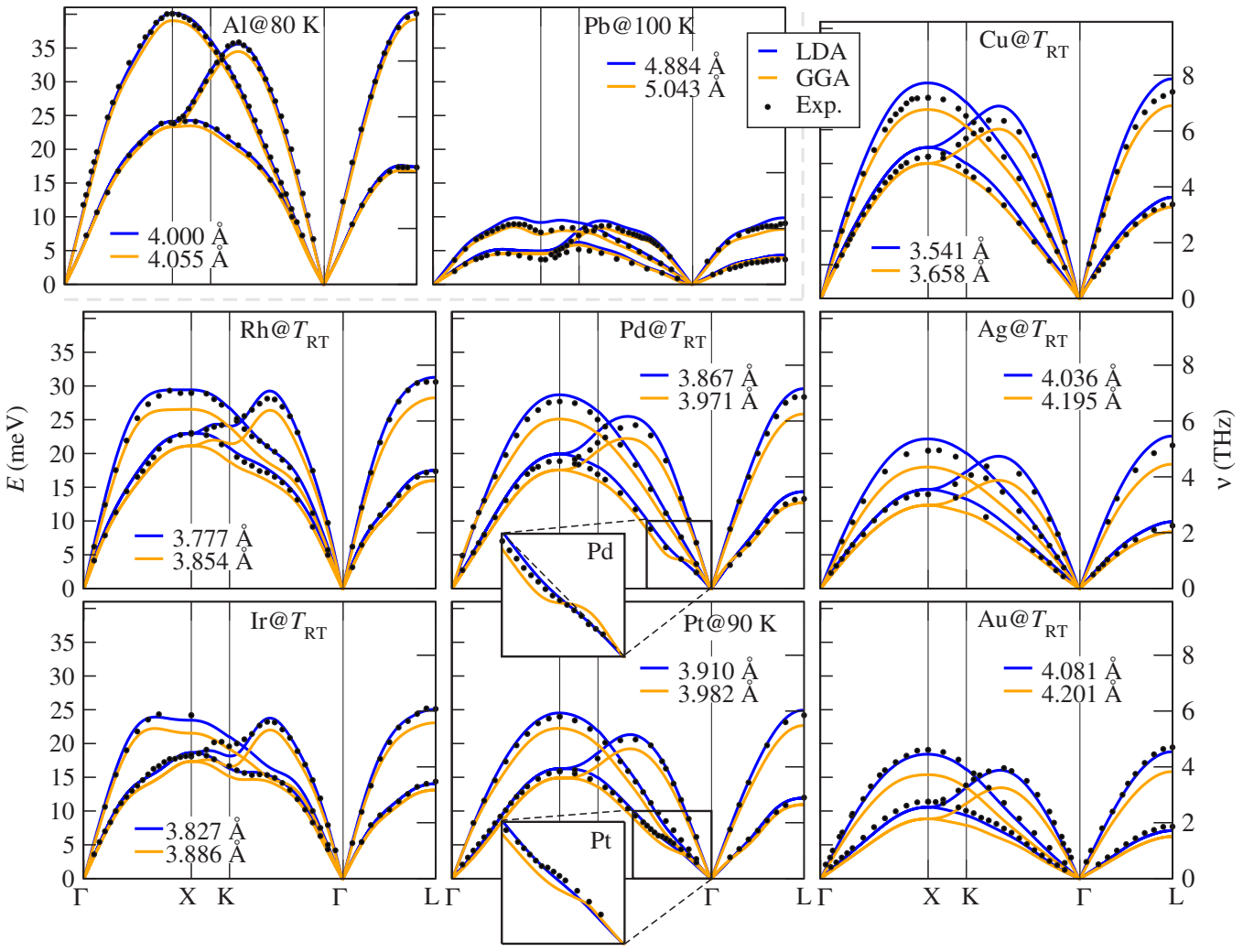

FIG. 11. (Color online) Phonon dispersion $\omega(\vec{q})$ $[E=h\nu=h\omega/(2\pi)$ with h the Planck constant] along some high symmetry directions calculated at the *ab initio* obtained equilibrium lattice constant for the given temperature. The corresponding lattice constant for each functional is given in the legend. The insets in the Pd and Pt phonon dispersions magnify the anomalies (the straight dashed line is a guide for the eye). A 5^3 supercell has been used for Pb and a 4^3 supercell for all other elements (see Sec. III B for further technical details; these parameters have also been used to obtain the results presented in all following figures). The experimental values are taken from Ref. 56 for Rh, from Ref. 59 for Ir, and from Ref. 41 for all other elements. Al and Pb are slightly separated to emphasize the Periodic Table correspondence of the other elements.

well with the LDA results from Refs. 59 and 60, where a sophisticated supercell approach has been used to include long-ranged force constants.

The phonon dispersion of Al has been in the focus of numerous studies.[9,17,52,55,61] It is, at first glance, similar to the phonon dispersion of Cu, Ag, and Au. However, a detailed inspection reveals anomalies for most branches. This is consistent with theoretical findings in Ref. 20. Our results for the LDA and GGA phonon dispersion of Al in Fig. 11 accurately reproduce these anomalies. It is noteworthy that a 4^3 supercell is the minimum cell size to resolve these anomalies.

Pb exhibits the most complex phonon dispersion among the investigated elements. This "complexity" became already apparent in Sec. IV C when inspecting the convergence with respect to the supercell size. The theoretical phonon dispersions computed for a large 5^3 supercell (500 atoms) excellently reproduce the experiment. We finally note that our LDA results for Pb agree well with a previous LDA linear response study.[42]

C. Thermal expansion

The thermal expansion can be calculated by employing Eq. (7). The linear thermal expansion ε and its coefficient α are defined as

$$\varepsilon(T) = \frac{a(T) - a(T_{\text{ref}})}{a(T_{\text{ref}})} \quad \text{and} \quad \alpha(T) = \frac{1}{a(T)} \frac{\partial a(T)}{\partial T}, \quad (16)$$

with a the equilibrium lattice constant. As reference temperature, we chose $T_{\text{ref}}=0$ K. The results are shown in Fig. 12. One should keep in mind, when comparing theory and experiment, that a comparison of ε and α, which are differential quantities, masks errors in the absolute values of the lattice constants. These deviations are listed in Table II.

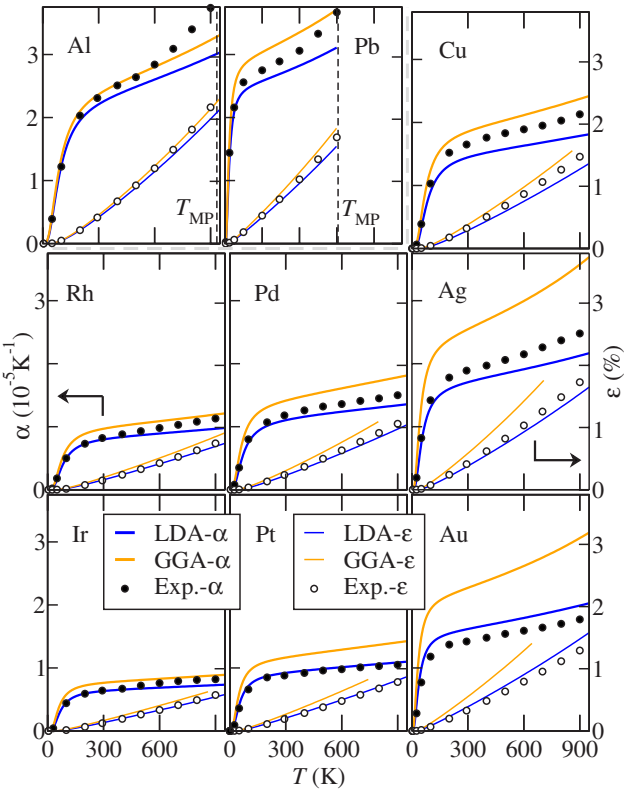

FIG. 12. (Color online) Linear thermal expansion ε (right axis) and its coefficient α (left axis) as a function of temperature T [Eq. (16)]. For Al and Pb, the experimental melting temperature T_{MP} is below the upper limit of the temperature interval considered here and included as a dashed line. The experimental data are taken from Ref. 47.

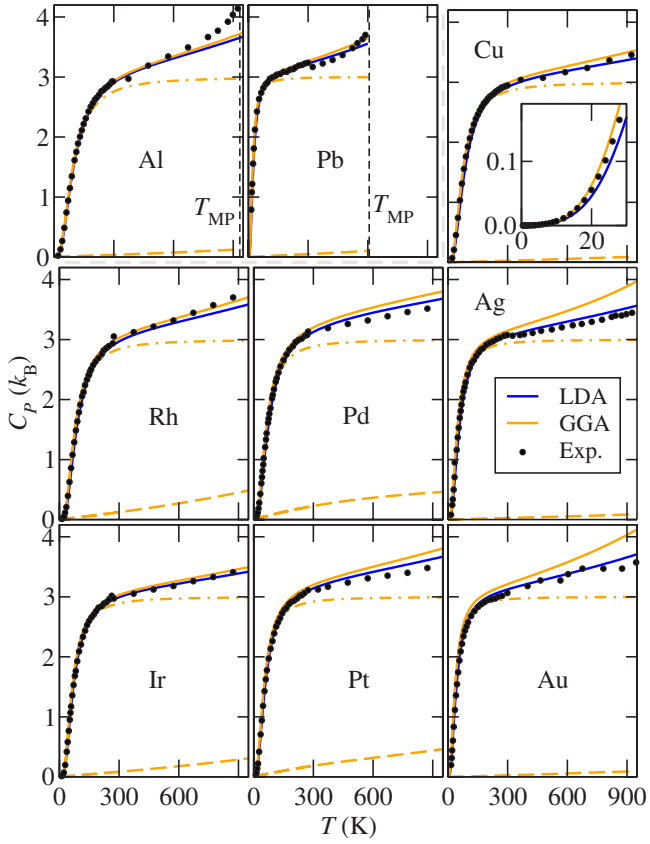

FIG. 13. (Color online) Heat capacity C_P at $P=0$ Pa as a function of temperature T in units of the Boltzmann constant k_B. For Al and Pb, the melting temperature T_{MP} is included (black dashed line). For GGA, the dashed-dotted lines show C_V and the dashed lines the electronic contribution C_P^{el}. The inset in the Cu heat capacity enlarges the low temperature region. The experimental data are taken from Ref. 62.

On average, we find a better agreement with experiment for the LDA than for the GGA results with GGA predicting a too large expansion. Moreover, the deviation between the GGA results and experiment shows a chemical trend among the transition metals. Filling up the *d* shell and increasing the atomic radius enlarges the error. The two most prominent examples are Ag and Au, where, in particular, the GGA α shows a significant deviation from experiment. The discrepancy of the Al α at temperatures below the melting point for LDA and GGA, which is due to anharmonic effects, will be discussed in more detail in the following section with a focus on the heat capacity.

In general, however, the probability that the experimental data lie in between or on the theoretical curves is high. Thus, similar to the results obtained for the phonon dispersions (Sec. V B), the deviation between LDA and GGA can be used to estimate the theoretical error bars and thus to obtain a fully *ab initio* confidence interval.

Previous *ab initio* studies on the thermal expansion of metals are rare. For the elements investigated here, we have found LDA studies for Al,[17,18] Cu,[8] and Ag.[16] In Ref. 8, a combined LDA and GGA study of thermodynamic properties for Cu has been performed. All these data are in good agreement with our corresponding LDA and/or GGA data.

D. Heat capacity

We now focus on the heat capacity at constant pressure C_P and fixed volume C_V. Experimentally, C_P is typically measured. Both of the calculated heat capacities and the experimental data taken from literature are shown in Fig. 13.

For C_P, which can be directly compared with experimental data, similar conclusions as in the previous section (thermal expansion) can be drawn: LDA yields an (astonishingly) good agreement with experiment. The GGA error has not such a clear chemical trend as in the case of the thermal expansion. However, we find again the largest deviations for the noble metals Ag and Au.

Our approach allows us to directly determine the electronic contributions to the heat capacity C_P^{el} (see dashed lines in Fig. 13). For Al, Pb, Cu, Ag, and Au, the electrons make only a small contribution to the heat capacity in the considered temperature range. For instance at 900 K, the contribution for Al, Cu, Ag, and Au is $\sim 0.1 k_B$ and $\sim 0.2 k_B$ for Pb. For Pb, however, already at 600 K the melting point is reached. The contribution at 600 K is $\sim 0.1 k_B$. This order of magnitude agrees, for instance, with the findings in Ref. 8 (for Cu) and Ref. 16 (for Ag). In contrast to these elements, C_P^{el} becomes significant for Pd, Pt, and Rh ($\sim 0.4 k_B$ at 900 K) and

for Ir ($\sim 0.3 k_B$ at 900 K). For Pd, Pt, Rh, and Ir, the origin of the significant electronic contribution are large electronic entropy effects due to a high electronic density of states near the Fermi level caused by partially occupied d states. Results for the electronic density of states of Pd, Pt, Rh, and Ir can be found, for instance, in Ref. 63.

Another noteworthy feature is observed for Al and Pb, which both reach the melting temperature already within the investigated temperature range. The LDA and GGA heat capacities for both elements are in good agreement up to temperatures $\sim 70\%$ of the melting point. For higher temperatures, the experimental heat capacity increases almost exponentially, while LDA and GGA heat capacities almost coincide and show a linear behavior. A similar dependence is observed also for the other elements at temperatures well above the upper temperature limit of 950 K considered here. We tentatively attribute this behavior to anharmonic effects, which become apparent at temperatures in the vicinity of the melting point. This conclusion is consistent with recent molecular dynamics and Monte Carlo studies employing empirical potentials for Al.[64] Within the quasiharmonic approach employed here, such anharmonic contributions are not included and will be a focus of a future study.

Finally, we note that our heat capacity results compare well with available previous calculations [Cu (Ref. 8) and Ag (Ref. 16)].

E. Free energy

Having computed the equilibrium volume $V_{\mathrm{eq}}(P,T)$ as a function of pressure and temperature, it is straightforward to obtain the free energy $F(P,T)$ from $F(V,T)$. The results are shown in Fig. 14 in comparison with values obtained from the CALPHAD approach.[2] For the elementary materials considered here, CALPHAD interpolates calorimetrically measured free energies as a function of temperature. In order to compare our DFT free energies $F^{\mathrm{DFT}}(P,T)$ to the CALPHAD free energies $F^{\mathrm{CA}}(P,T)$, we shift both

$$\bar{F}^{\mathrm{DFT}}(P,T) = F^{\mathrm{DFT}}(P,T) - F^{\mathrm{DFT}}(P,T_{\mathrm{ref}}), \tag{17}$$

$$\bar{F}^{\mathrm{CA}}(P,T) = F^{\mathrm{CA}}(P,T) - F^{\mathrm{CA}}(P,T_{\mathrm{ref}}). \tag{18}$$

We follow the CALPHAD approach and choose a finite temperature as the reference ($T_{\mathrm{ref}}=200$ K). The reason of using a temperature different from 0 K is the lack of accurate experimental data at low temperatures.

The results for the free energy (Fig. 14) follow closely the trends found for the thermal expansion and the heat capacity. For all elements, the LDA results are in good agreement with the CALPHAD data, whereas the GGA error exhibits the same chemical trend among the transition metals: Filling up the d shell and increasing the atomic radius, the GGA deviation from experiment increases and cumulates again in significant errors for the noble metals Ag and Au. Similar to the heat capacity, a considerable contribution to the free energy of Pd, Pt, Rh, and Ir stems from electronic excitations (electronic entropy).

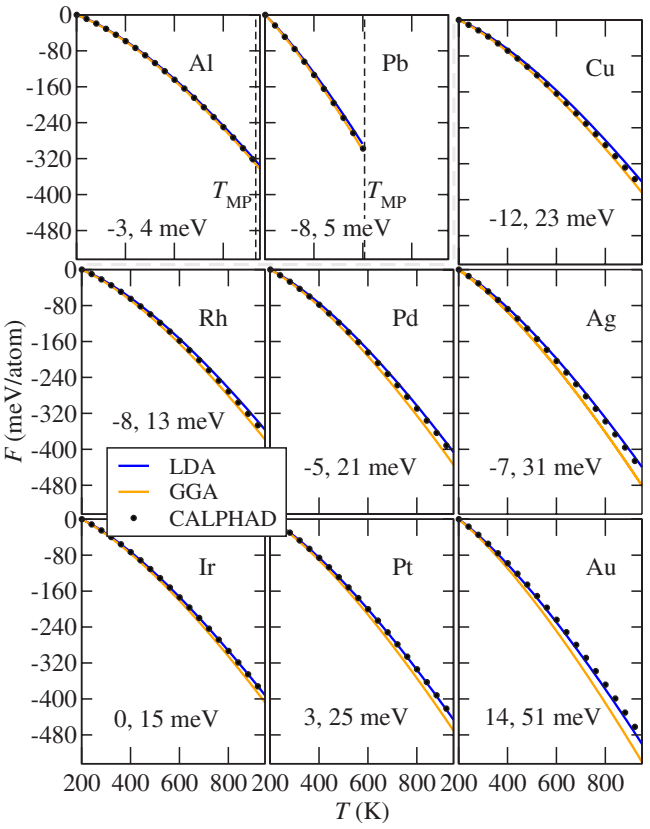

FIG. 14. (Color online) Free energy F at $P=0$ Pa as a function of temperature T for both functionals in comparison with values obtained with the CALPHAD method (using THERMOCALC version Q and the "PURE4 -SGTE Pure Elements Database"). For Al and Pb, the melting temperature T_{MP} is included (dashed line). The numbers inside each graph give $F^{\mathrm{CA}}-F^{\mathrm{DFT}}$ at $T=900$ K ($T=600$ K for Pb) for LDA and GGA (1 meV/atom $\approx$ 0.023 kcal/mol).

VI. COMPARISON BETWEEN THEORY AND EXPERIMENT: MIXED APPROACH

When analyzing the (small but often not negligible) errors between theory (in particular, GGA) and experiment, the question arises to what degree these are related to the considerable errors in the $T=0$ K quantities (Sec. V A). To address this issue, we have used different approaches depending on the quantity to be analyzed.

For the phonon dispersion, we simply have to replace the *ab initio* calculated equilibrium lattice constant (Sec. V B) by the experimental lattice constant at a given temperature.[9,65,66] Figure 15 shows the effect for Rh as an example. The difference between the LDA and GGA results is reduced and thus the averaged deviation from experiment decreases slightly, in particular, for GGA. A further interesting consequence is that replacing the fully theoretical lattice constants by the experimental lattice constants flips the LDA and GGA results, i.e., while in Fig. 15(a) (theoretical lattice constant) the LDA (GGA) results give rise to an upper (lower) bound of the experimental data, in Fig. 15(b) (experimental lattice constant) the opposite behavior is found. We find that this behavior can be generalized to all other elements in this study. The same trend has been reported for Al (Ref. 9) and Cu (Refs. 8 and 9).

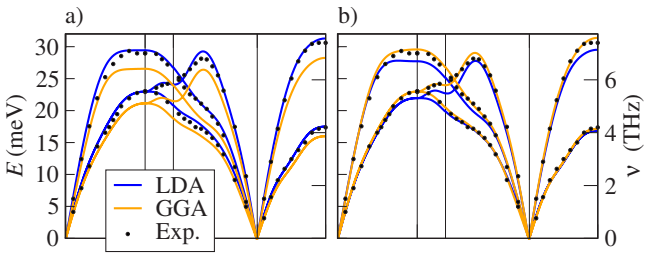

FIG. 15. (Color online) Phonon dispersion of Rh at room temperature (4^3 supercell) calculated (a) fully *ab initio* at lattice constants as given for Rh in Fig. 11 and (b) at the experimental room temperature lattice constant of 3.803 Å.

In order to estimate the effect of the error in the $T=0$ K quantities on thermodynamic properties such as the thermal expansion, heat capacity, and free energy, we have applied the following approach: We have split the free energy $F(V,T)$ into

$$F = \underbrace{E^{\mathrm{tot}}(V,T=0\ \mathrm{K}) + E^{\mathrm{zero}}}_{:=E^{\mathrm{exp}}(V,T=0\ \mathrm{K})} + \underbrace{\bar{F}^{\mathrm{el}} + F^{\mathrm{vib}} - E^{\mathrm{zero}}}_{:=F^{\mathrm{th}}(V,T).} \qquad (19)$$

Here, $E^{\mathrm{zero}}=E^{\mathrm{zero}}(V)$ is defined to be the energy contribution of zero-point vibrations and $\bar{F}^{\mathrm{el}}$ is given by Eq. (8). With the decomposition of Eq. (19) at hand, we have been able to parametrize the $T=0$ K energy surface $E^{\mathrm{exp}}(V,T=0\ \mathrm{K})$ according to Eq. (11) using the experimental data for a, B, and B' and to calculate $F^{\mathrm{th}}(V,T)$ fully *ab initio*. For elements, where no experimental data were available for B', we have used the average of the LDA and GGA value given in Table II. In the following, we call this approach of combining the experimental $T=0$ K potential energy surface with the fully *ab initio* thermal energy contribution F^{th} as mixed approach.

We have applied this approach to the thermal expansion, heat capacity, and free energy (Figs. 16–18, respectively). These figures show general trends for all properties. Most remarkable is the significant reduction of the discrepancy between GGA results and experiment and the largely reduced difference between the LDA and GGA results. The only exception is Pb, where the difference between LDA and GGA becomes slightly larger. This effect is strongest for the thermal expansion (Figs. 12 and 16) and the heat capacity (Figs. 13 and 17), but also applies to the free energy (Figs. 14 and 18).

Let us now focus on specific characteristics of the different quantities: The GGA thermal expansion parameters are shifted downward for all elements, resulting in a significantly improved agreement with experiment. The main source of this downshift is the replacement of the (too soft) GGA bulk modulus (see Table II) by the correct experimental modulus. For the same reason, the mixed approach reduces the GGA heat capacity and the GGA free energy. The effect is most significant for Ag and Au. The trend for LDA is inverse and smaller in its magnitude. The reason is that the (slightly too hard) LDA bulk modulus is replaced by the correct experimental one.

VII. CONCLUSIONS

Based on extensive convergence checks, we have studied the accuracy of two popular DFT XC functionals (LDA and GGA-PBE) in predicting a wide range of thermodynamic material properties. The study has been performed for a systematic and comparable set of materials: elementary nonmagnetic metals that are thermodynamically stable at $T=0$ K in the fcc crystal phase. The large set of nine elements allows us to derive systematic trends, which we expect to hold also for related elements and alloys.

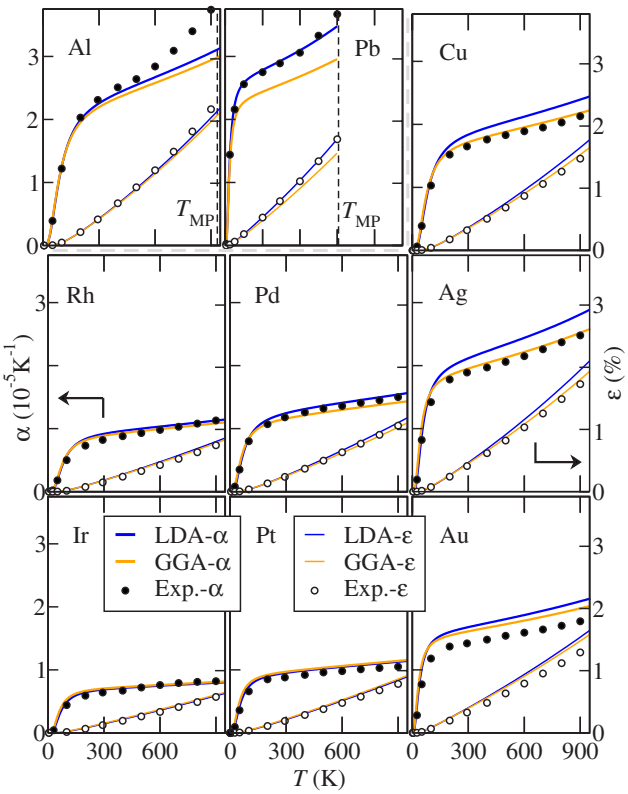

FIG. 16. (Color online) Linear thermal expansion ε (right axis) and its coefficient α (left axis) as a function of temperature T using the mixed approach [see Eq. (19) and text]. For a comparison with the fully *ab initio* data, see Fig. 12.

For the phonon dispersion, which is a key quantity to calculate thermodynamic properties, no general preference of LDA or GGA exists. Some of the investigated metals (Au,Ir) are better described by LDA, others (Pb) by GGA. However, the experimental data for most elements lie in between the LDA and GGA results. For the thermodynamic quantities, such as thermal expansion, heat capacity, or the free energy, which effectively average over the phonon dispersion, LDA generally yields a (slightly) better agreement with experiment than GGA. Exceptions are Al and Pb, for which both functionals give almost identical results. An interesting observation of these studies is that LDA and GGA give a generic upper and lower bound to the experimental data. This allows us to construct fully *ab initio* error bars for the theoretically computed thermodynamic data. An analysis of the error bars allows us to quickly identify problematic cases like the noble metals Ag and Au (full d shell), for which comparatively large deviations between LDA and GGA have been found for all quantities considered. The thus identified problematic cases might be used to construct and/or validate further XC functionals.

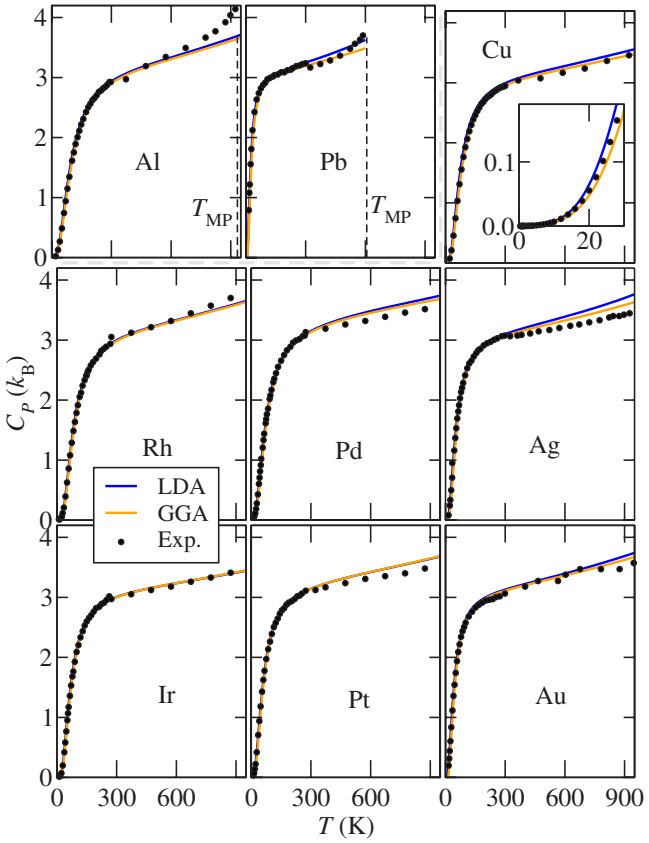

FIG. 17. (Color online) Heat capacity C_P at constant pressure as a function of temperature T using the mixed approach. For a comparison with the fully *ab initio* data, see Fig. 13.

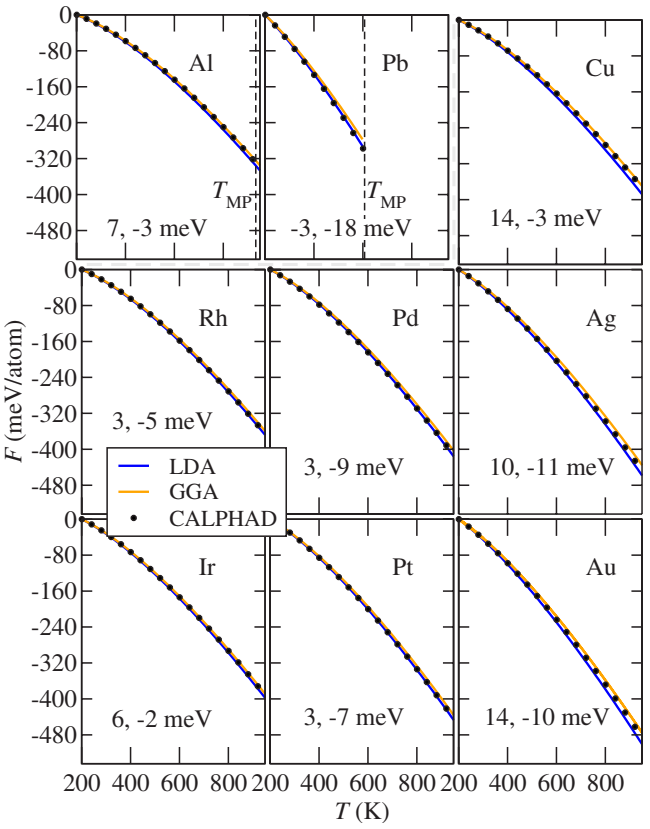

FIG. 18. (Color online) Free energy F at $P=0$ Pa as a function of temperature T. The numbers inside each graph give $F^{CA}-F^{DFT}$ at $T=900$ K ($T=600$ K for Pb) for LDA and GGA (1 meV/atom ≈ 0.023 kcal/mol). For a comparison with the fully *ab initio* data, see Fig. 14.

We believe that the property of LDA and GGA to bound experimental thermodynamic data holds not only for the elements studied here, but is a general feature valid also for other crystal structures and alloys. In this case, the availability of *ab initio* error bars could be used to quantify the predictive accuracy of DFT even for materials for which experimental data are incomplete or lacking.

An in-depth analysis of the deviation between theory and experiment has shown that the errors are largely due to the limited accuracy of the $T=0$ K potential energy obtained from the LDA and GGA functionals. These errors, which are caused, e.g., by the overbinding in LDA (yielding slightly too small lattice constants and too hard bulk moduli), are well known and have been extensively studied. Removing this source of error by replacing the $T=0$ K energy surface by experimental data leads to a large and systematic reduction in the error between DFT and experiment. It also largely reduces the difference between the LDA and GGA results. Since, as discussed above, this difference can be regarded as an *ab initio* error bar, the predictive accuracy significantly increases. This opens an interesting route to systematically (and fully theoretically) improve the accuracy of thermodynamic data: The $T=0$ K potential energy can be described by using the elementary unit cell. Since this cell contains typically only a few atoms (for the metals studied here only a single atom), *ab initio* approaches going beyond the LDA and/or GGA level should be feasible and provide an accurate description of the $T=0$ K surface. The finite temperature contributions, requiring larger system sizes to capture long-range force constants, can then be calculated with sufficient accuracy with LDA and/or GGA DFT.

ACKNOWLEDGMENT

We wish to acknowledge the financial support by the Helmholtz-Gemeinschaft under the project VIVIMAT (Virtuelles Institut für virtuelles Materialdesign).

[1] T. B. Massalski, Metall. Trans. A **20**, 1295 (1989).
[2] L. Kaufman and H. Bernstein, *Computer Calculation of Phase Diagrams* (Academic, New York, 1970).
[3] N. Saunders and A. P. Miodownik, *Calphad (Calculation of Phase Diagrams): A Comprehensive Guide* (Pergamon, Oxford, 1998).
[4] P. Hohenberg and W. Kohn, Phys. Rev. **136**, B864 (1964).
[5] J. Hafner, C. Wolverton, and G. Ceder, MRS Bull. **31**, 659 (2006).
[6] In principle, a systematically improvable set of XC functionals could be constructed by employing Levy-Görling (Ref. 67) perturbation theory. However, even the first order (the optimized effective potential approach) is computationally a few orders of magnitude more expensive than conventional functionals based on LDA and GGA and for total energy calculations much less accurate.
[7] S. Mehta, G. D. Price, and D. Alfè, J. Chem. Phys. **125**, 194507 (2006).
[8] S. Narasimhan and S. de Gironcoli, Phys. Rev. B **65**, 064302 (2002).
[9] F. Favot and A. Dal Corso, Phys. Rev. B **60**, 11427 (1999).
[10] P. E. A. Turchi *et al.*, CALPHAD: Comput. Coupling Phase Diagrams Thermochem. **31**, 4 (2007).
[11] Y. Wang, S. Curtarolo, C. Jiang, R. Arroyave, T. Wang, G. Ceder, L.-Q. Chen, and Z.-K. Liu, CALPHAD: Comput. Coupling Phase Diagrams Thermochem. **28**, 79 (2004).
[12] N. D. Mermin, Phys. Rev. **137**, A1441 (1965).
[13] A. van de Walle and G. Ceder, Rev. Mod. Phys. **74**, 11 (2002).
[14] J. M. Sanchez, F. Ducastelle, and D. Gratias, Physica A **128**, 334 (1984).
[15] I. A. Abrikosov and B. Johansson, Phys. Rev. B **57**, 14164 (1998).
[16] J. Xie, S. de Gironcoli, S. Baroni, and M. Scheffler, Phys. Rev. B **59**, 965 (1999).
[17] A. Debernardi, M. Alouani, and H. Dreyssé, Phys. Rev. B **63**, 064305 (2001).
[18] A. A. Quong and A. Y. Liu, Phys. Rev. B **56**, 7767 (1997).
[19] V. L. Moruzzi, J. F. Janak, and K. Schwarz, Phys. Rev. B **37**, 790 (1988).
[20] D. C. Wallace, *Thermodynamics of Crystals* (Dover, New York, 1998).
[21] M. J. Gillan, J. Phys.: Condens. Matter **1**, 689 (1989).
[22] H. Hellmann, *Einführung in die Quantenchemie* (Deuticke, Leipzig, 1937).
[23] R. P. Feynman, Phys. Rev. **56**, 340 (1939).
[24] P. E. Blöchl, Phys. Rev. B **50**, 17953 (1994).
[25] G. Kresse and J. Furthmüller, Phys. Rev. B **54**, 11169 (1996).
[26] G. Kresse and D. Joubert, Phys. Rev. B **59**, 1758 (1999).
[27] P. Blaha, K. Schwarz, G. Madsen, D. Kvasnicka, and J. Luitz, *WIEN2k, An Augmented Plane + Local Orbitals Program for Calculating Crystal Properties* (Technische Universität Wien, Wien, Austria, 2001).
[28] D. M. Ceperley and B. J. Alder, Phys. Rev. Lett. **45**, 566 (1980).
[29] J. P. Perdew and A. Zunger, Phys. Rev. B **23**, 5048 (1981).
[30] J. P. Perdew, K. Burke, and M. Ernzerhof, Phys. Rev. Lett. **77**, 3865 (1996).
[31] H. J. Monkhorst and J. D. Pack, Phys. Rev. B **13**, 5188 (1976).
[32] The unit kp·atom takes the inverse relation between real and reciprocal spaces into account. Thus, the actual number of (reducible) k points in the considered cell is obtained by dividing kp·atom by the number of atoms in the cell.
[33] F. D. Murnaghan, Proc. Natl. Acad. Sci. U.S.A. **30**, 244 (1944).
[34] K. Parlinski, Z. Q. Li, and Y. Kawazoe, Phys. Rev. Lett. **78**, 4063 (1997).
[35] G. Kresse, J. Furthmüller, and J. Hafner, Europhys. Lett. **32**, 729 (1995).
[36] D. Alfè, G. D. Price, and M. J. Gillan, Phys. Rev. B **64**, 045123 (2001).
[37] M. Methfessel and A. T. Paxton, Phys. Rev. B **40**, 3616 (1989).
[38] G. Kresse and J. Furthmüller, *VASP the guide* (Technische Universität Wien, Wien, Austria, 2005), cms.mpi.univie.ac.at/vasp/vasp.pdf.
[39] In VASP, such an augGrid size is achieved for a high precision calculation (flag: PREC=HIGH).
[40] This corresponds to a high precision calculation with an additional support grid in VASP (flag: ADDGRID=TRUE).
[41] *Metals: Phonon States, Electron States and Fermi Surfaces*, Landolt-Börnstein, New Series, Group III, Vol. 13, Pt. a (Springer-Verlag, Berlin, 1981).
[42] S. de Gironcoli, Phys. Rev. B **51**, 6773 (1995).
[43] K. A. Gschneidner, Solid State Phys. **16**, 275 (1964).
[44] P. S. Ho and A. L. Ruoff, J. Appl. Phys. **40**, 3151 (1969).
[45] In principle, it is also possible to obtain the theoretical Grüneisen parameter from the calculated C_V dependence analogous to the experiment. Using this value, the assumption of the approximate Mie-Grüneisen equation of state could be evaluated element specifically.
[46] Constant atomic sphere radii have been used for each element ranging from 2.3 to 2.5 Bohr radius. An $18\times18\times18$ k-point mesh has been used and the product of the atomic sphere radius and the maximum reciprocal space vector, $R_{\mathrm{MT}}k_{\mathrm{max}}$, has been set to 10. The maximum ℓ value for the waves inside the atomic spheres and the largest reciprocal vector $\vec{G}$ in the charge Fourier expansion have been set to $\ell_{\mathrm{max}}=12$ and $\vec{G}_{\mathrm{max}}=14$ (Bohr radius)$^{-1}$, respectively. Relativistic effects have been included fully within the atomic spheres and using the scalar relativistic approximation in the valence region.
[47] Y. S. Touloukian, R. K. Kirby, R. E. Taylor, and P. D. Desai, *Thermophysical Properties of Matter* (IFI/Plenum, New York, 1975), Vol. 12.
[48] J. A. Rayne, Phys. Rev. **118**, 1545 (1960).
[49] E. Walker, J. Ashkenazi, and M. Dacorogna, Phys. Rev. B **24**, 2254 (1981).
[50] R. E. Macfarlane, J. A. Rayne, and C. K. Jones, Phys. Lett. **20**, 234 (1966).
[51] J. H. Rose, J. R. Smith, F. Guinea, and J. Ferrante, Phys. Rev. B **29**, 2963 (1984).
[52] S. Y. Savrasov and D. Y. Savrasov, Phys. Rev. B **54**, 16487 (1996).
[53] L. Vočadlo, D. Alfè, G. D. Price, and M. J. Gillan, J. Chem. Phys. **120**, 2872 (2004).
[54] A. A. Quong, Phys. Rev. B **49**, 3226 (1994).
[55] R. Bauer, A. Schmid, P. Pavone, and D. Strauch, Phys. Rev. B **57**, 11276 (1998).
[56] A. Eichler, K.-P. Bohnen, W. Reichardt, and J. Hafner, Phys. Rev. B **57**, 324 (1998).
[57] T. Takezawa, H. Nagara, and N. Suzuki, Phys. Rev. B **71**, 012515 (2005).
[58] I. Y. Sklyadneva, A. Leonardo, P. M. Echenique, S. V. Eremeev, and E. V. Chulkov, J. Phys.: Condens. Matter **18**, 7923 (2006).

[59] R. Heid, K.-P. Bohnen, K. Felix, K. M. Ho, and W. Reichardt, J. Phys.: Condens. Matter **10**, 7967 (1998).
[60] R. Heid, K.-P. Bohnen, and K. M. Ho, Phys. Rev. B **57**, 7407 (1998).
[61] L. Vočadlo and D. Alfè, Phys. Rev. B **65**, 214105 (2002).
[62] Y. S. Touloukian and E. H. Buyco, *Thermophysical Properties of Matter* (IFI/Plenum, New York, 1970), Vol. 4.
[63] P. E. A. Turchi, V. Drchal, and J. Kudrnovsky, Phys. Rev. B **74**, 064202 (2006).
[64] M. Forsblom, N. Sandberg, and G. Grimvall, Phys. Rev. B **69**, 165106 (2004).
[65] A. van de Walle and G. Ceder, Phys. Rev. B **59**, 14992 (1999).
[66] A. Dal Corso and S. de Gironcoli, Phys. Rev. B **62**, 273 (2000).
[67] A. Görling and M. Levy, Phys. Rev. A **50**, 196 (1994).